Inorganic Chemistry

Article

pubs.acs.org/IC

Hydration Thermodynamics of the Proton Conducting Oxygen-Deficient Perovskite Series $BaTi_{1-x}M_xO_{3-x/2}$ with M = In or Sc

Tor Svendsen Bjørheim,*[†] Seikh M. H. Rahman,[‡] Sten G. Eriksson,[‡] Christopher S. Knee,[‡] and Reidar Haugsrud[†]

[†]Center for Materials Science and Nanotechnology, Department of Chemistry, University of Oslo, FERMiO Gaustadalléen 21, 0349 Oslo, Norway

[‡]Department of Chemical and Biological Engineering, Chalmers University of Technology, Göteborg 412 58, Sweden

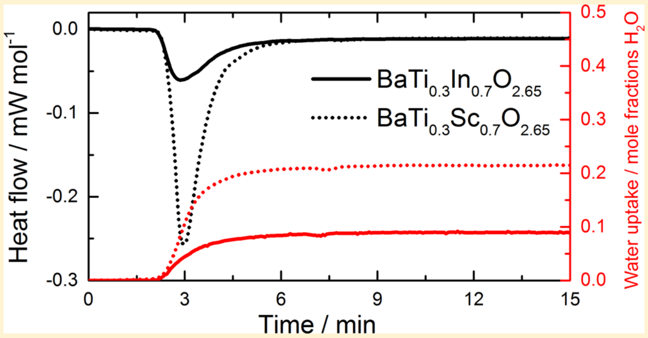

ABSTRACT: This article establishes the effect of structure and composition on water uptake and the hydration and proton transport properties of the oxygen-deficient perovskite series $BaTi_{1-x}(In,Sc)_xO_{3-x/2}$, with $0.2 \leq x \leq 0.7$. The equilibrium water uptake is determined by thermogravimetry, while combining thermogravimetry with differential scanning calorimetry allows for *direct* determination of the materials' hydration thermodynamics. Proton and oxide ion transport properties are characterized by means of ac impedance measurements up to 1000 °C. In general, the hydration thermodynamics of the scandates are more favorable than that of the indates and are also affected by changes in crystal structure throughout the series. The more favorable hydration thermodynamics of cubic scandates increase their proton conductivity at higher temperatures compared to their indate counterparts. In contrast to the $BaTi_{1-x}In_xO_{3-x/2}$ series, the $BaTi_{1-x}Sc_xO_{3-x/2}$ ($0.5 \leq x \leq 0.7$) materials retain their cubic structures upon full saturation by protons and show no signs of chemical instability upon exposure to 1 atm $H_2O(g)$ down to 100 °C. The $BaTi_{1-x}Sc_xO_{3-x/2}$ materials with $0.5 \leq x \leq 0.7$ may therefore find application in, for instance, steam electrolysis or similar processes involving high water vapor pressures.

1. INTRODUCTION

Oxides with the perovskite structure exhibit large flexibility in oxygen stoichiometry. Oxygen deficiency, in the form of oxygen vacancies, may be either an inherent part of the oxide structure or formed as the charge compensating defect upon introduction of lower valence ions, a process commonly termed acceptor doping. Under wet conditions these oxygen vacancies may interact with water vapor

$$H_2O(g) + O_O^{\times} + v_O^{\bullet\bullet} \leftrightarrows 2OH_O^{\bullet} \tag{1}$$

Protons are in this way introduced as point defects. Protons may be highly mobile at elevated temperatures, and ceramics with appreciable levels of proton conductivity find usage as, for instance, electrolytes in proton conducting solid oxide fuel cells and hydrogen separation membranes.

In an ideal case where oxygen vacancies and protons are the majority defects, charge compensating a relatively small amount of acceptor dopants, their concentration can be derived based on the thermodynamics of the defect reaction in eq 1

$$K_{Hydr} = \frac{[OH_O^{\bullet}]^2}{[v_O^{\bullet\bullet}][O_O^{\times}]p_{H_2O}} = \exp\left(\frac{\Delta_{Hydr}S^{\circ}}{R}\right)\exp\left(-\frac{\Delta_{Hydr}H^{\circ}}{RT}\right) \tag{2}$$

where $\Delta_{Hydr}S^{\circ}$ and $\Delta_{Hydr}H^{\circ}$ are the standard hydration entropy and enthalpy, respectively. This relation is strictly valid only when the concentration of defects is sufficiently low that there is no interaction between any of the defects, i.e., within the so-called dilute limit. There have been extensive efforts to understand the compositional dependence of the hydration thermodynamics (eqs 1 and 2) in order to engineer materials with a high concentration of protonic charge carriers at elevated temperatures. For ABO_3 perovskites, $\Delta_{Hydr}H^{\circ}$ has been correlated to the electronegativity difference of the A- and B-site cations (more exothermic with decreasing difference),[1] which has been suggested to reflect the basicity of the oxide. $\Delta_{Hydr}H^{\circ}$ has also been shown to become more exothermic when the Goldschmidt tolerance factor is lower than 1,[2] reflecting that perovskites with the largest deviations from the cubic structure tend to display the most exothermic $\Delta_{Hydr}H^{\circ}$. Whether the latter correlation actually reflects a structural dependency on the hydration thermodynamics or stems from the fact that the tolerance factor is derived from the cation radii and is related to their electronegativity can be debated. Isostructural systems with varying electronegativity difference of the cations could be a good test of the latter correlation.

Numerous oxides dissolve protons according to eq 1 and consequently display protonic conductivity. The saturation level in proton concentration is given by the solubility limit of

Received: December 18, 2014
Published: March 2, 2015

DOI: 10.1021/ic503006u
Inorg. Chem. 2015, 54, 2858−2865

the acceptor dopant and is generally around 15−20 mol %, like for the alkaline-earth cerates and zirconates, and even considerably lower, as often encountered for nonperovskite structured oxides with acceptor solubility below 5 mol %. Certain ABO_3 perovskites, however, display almost complete solid solubility of both isovalent and lower valent cations. By substituting four valent cations on the B site, B^{IV}, with a trivalent cation, B^{III}, oxygen vacancies form as a charge compensating defect ($A^{II}B^{III}_xB^{IV}_{1-x}O_{3-\delta}$). Upon further substitution of B^{III}, the oxygen vacancies eventually order in parallel rows, principally defining the phase transition from a 2:4 $A^{II}B^{IV}O_{3-\delta}$ perovskite to a brownmillerite-structured oxide, $ABO_{2.5}$. Within these solid solubility regions, the high concentration of oxygen vacancies, and potentially also of protons, may offer high proton conductivities. However, in this respect, the literature has shown that there generally is a balance between favorable and adverse consequences of such highly defective crystal lattices. Phenomena such as transitions of the crystal structure, order−disorder transitions, and formation of defect complexes (trapping) may come into play across the compositional range, all challenging the classical approaches of treating the defect chemistry and transport mechanisms of these materials. Investigations of these phenomena through the compositional range of a solid solution and of how thermodynamics and transport develop with defect concentrations beyond the dilute limit are, accordingly, of great interest both from fundamental and technological perspectives.

$BaTi_{1-x}In_xO_{3-x/2}$ and $BaTi_{1-x}Sc_xO_{3-x/2}$ represent such highly oxygen deficient perovskite series of materials. Both materials have been shown to hydrate in water vapor containing atmospheres, and display significant proton conductivity at intermediate temperatures.[3−10]

2. $BaTi_{1-X}M_XO_{3-X/2}$ (M = In, Sc) SERIES OF MATERIALS

$BaTi_{1-x}In_xO_{3-x/2}$ may be treated as acceptor (In) doped $BaTiO_3$ where In is charge compensated by oxygen vacancies. Alternatively, with the brownmillerite as reference state, the series may be described as donor (Ti) doped $Ba_2In_2O_5$ where Ti is charge compensated by O^{2-} interstitials, i.e., $BaTi_{1-x}In_xO_{2.5+x/2}$. This "arbitrary" choice of reference state could be avoided by redefining the defective oxide as the perfect state, with fractional occupation of O lattice sites by O^{2-} or OH^- ions as suggested by Norby.[11] For our solid−solution series, however, this would lead to a gradually changing reference state—and thus nomenclature—with increasing Sc/In content. We therefore rather adopt the traditional nomenclature of acceptor-doped oxides throughout this article. From the electroneutrality condition

$$[M'_{Ti}] = 2[v_O^{\bullet\bullet}] + [OH_O^{\bullet}] \tag{3}$$

and by accounting for site conservation

$$[O] = [v_O^{\bullet\bullet}] + [OH_O^{\bullet}] + [O_O^{\times}] \tag{4}$$

the hydration equilibrium constant (eq 2) be rewritten as

$$K_{Hydr} = \frac{([OH_O^{\bullet}])^2}{(0.5([M'_{Ti}] - OH_O^{\bullet}))([O] - 0.5[M'_{Ti}] - 0.5[OH_O^{\bullet}]])p_{H_2O}} \tag{5}$$

where $[M'_{Ti}]$ is the In or Sc concentration and [O] is the concentration of lattice oxygen sites.

Undoped $Ba_2In_2O_5$ undergoes phase transitions above 925 °C, where the oxygen sublattice disorders,[12] and the oxygen ion conductivity reaches levels comparable to YSZ and GDC.[13] Minor amounts of tri-, tetra-, penta-, or hexavalent dopants (Y, Sc, Ga, Ti, Zr, Ce, Hf, Si, P, W[3,5,8,9,13−16]) lower the transition temperature and stabilize the cubic, disordered structure. Pure $Ba_2In_2O_5$ also hydrates to form the oxy−hydroxide $Ba_2In_2O_4(OH)_2$ which crystallizes in a tetragonal structure.[4,17] The proton conductivity of this hydrated phase is, however, modest.[4,17−19] Stabilization of the cubic perovskite structure by the above-mentioned dopants increases the proton conductivity of the solid solutions. The most widely studied solid solution series with respect to proton transport is by far $BaTi_{1-x}In_xO_{3-x/2}$.[3−8,14,20] Jayaraman et al.[3] showed that compositions with $0.925 > x > 0.85$ have a tetragonal structure, while those with $x < 0.85$ adopt the cubic perovskite structure with disordered oxygen vacancies at room temperature. The maximum water uptake of the series increases with increasing x, and all compositions reach complete saturation at lower temperatures.[4] On the basis of curve fitting of hydration isobars of compositions with $x = 0.4−0.8$, Quarez et al.[5] concluded that the hydration enthalpy becomes less favorable (less exothermic) with increasing x while the hydration entropy becomes less negative in the same direction, ranging from around −60 to −100 kJ/mol and from −110 to −190 J/mol·K, respectively. Further, the series was shown to be dominated by protonic conductivity up to 450 °C, which increases with decreasing Ti content, and peaks at 1.1×10^{-3} S cm^{-1} at 450 °C for $BaTi_{0.2}In_{0.8}O_{2.6}$. Among similar lines of compositions, Rahman et al.[9,10] investigated the structural and proton transport properties of the $BaTi_{1-x}Sc_xO_{3-x/2}$ series with $x = 0.1−0.8$. Compositions with $x = 0.5−0.7$ were found to adopt disordered cubic perovskite structures, while those with $x = 0.1−0.2$ were reported to take on a hexagonal perovskite-related structure.[20] The highest proton conductivity of $\sim 2 \times 10^{-3}$ S cm^{-1} was found for the cubic $x = 0.7$ sample. They moreover reported the proton conductivity to extend to slightly higher temperatures than for the corresponding In members, indicative of an effect of Sc on the hydration properties of the series. However, the reported hydration enthalpy and entropy of −100 ± 5 kJ/mol and −160 ± 10 J/mol·K, respectively, from curve fitting of conductivity data for $BaTi_{0.5}Sc_{0.5}O_{2.75}$[9] are both in the range of those found for the In members, and no general trend was reported. For ABO_3 perovskites with moderate acceptor concentrations, effects of type of acceptor dopant on the hydration and proton transport properties may be attributed to trapping of protons and/or oxygen vacancies by the effectively negatively charged acceptor. In highly deficient oxide systems such as $BaTi_{1-x}M_xO_{3-x/2}$ (M = In, Sc), however, the effect of variations in the cation composition may be more complex as the materials resemble solid solutions where oxygen sites surrounding the acceptor at some point become indistinguishable from sites surrounding the host cations.

In this article, we aim to (1) establish the compositional dependence of the hydration thermodynamics of the cubic $BaTi_{1-x}M_xO_{3-x/2}$ (M = In, Sc) series, hereafter denoted BTS*X* and BTI*X* where *X* represents the mol % of dopant, (2) investigate the effect of the cubic to hexagonal phase transition on the hydration properties of $BaTi_{1-x}ScO_{3-x/2}$, (3) compare direct experimental (TG-DSC method) and indirect determination of thermodynamic hydration properties, and finally (4) investigate correlations between the hydration properties and the proton mobility. Defect thermodynamics and transport properties are investigated by combining thermogravimetric (TG) measurements of water uptake, direct measurements by means of combined thermogravimetry and differential scanning calorimetry (TG-DSC), and electrical characterization.

3. EXPERIMENTAL SECTION

3.1. Materials Synthesis. The BTS20−70 series and BTI50 compositions investigated in this work are the same as those employed in refs 7, 9, and 10. For completeness, we also synthesized and characterized BTI70 for this work.

All compositions were synthesized by a conventional solid state sintering method by mixing stoichiometric amounts of the starting powders, as described in refs 9 and 10. For the $BaTi_{1-x}Sc_xO_{3-x/2}$ phases (x = 0.2, 0.5, 0.6, 0.7), $BaCO_3$ (Sigma-Aldrich, ≥99%), TiO_2 (Merck, 99.8%), and Sc_2O_3 (Sigma-Aldrich, 99.9%) were used as starting powders. The final sintering temperature for BTS20 was 1400 °C, while BTS50, BTS60, and BTS70 samples were sintered at 1550 °C.[10]

$BaTi_{0.5}In_{0.5}O_{2.75}$ (BTI50) and $BaTi_{0.3}In_{0.7}O_{2.65}$ (BTI70) were prepared from $BaCO_3$ (Sigma-Aldrich, 99.99%), TiO_2 (Alfa Aesar, 99.8%), and In_2O_3 (Fluka, 99.99%). $BaCO_3$ and TiO_2 were dried in a heating cabinet at 200 °C overnight, while In_2O_3 was dried at 700 °C for 1 h prior to synthesis. The powders were pressed to disk samples and calcined at 1000, 1200, and 1400 °C for 12 h in ambient air with crushing/mixing and subsequent drying in between each calcination step.

XRD analyses (XRD, Bruker D8 Discover, Cu Kα, Bragg−Brentano) of the final BTI70 powders were consistent with a cubic perovskite structure ($Pm\bar{3}m$) and showed no indications of secondary phases. Detailed analyses on the phase purity and structural investigations of the synthesized BTI50 and BTS20−70 compositions can be found in refs 7, 9, and 10. Similar to BTI70, XRD analyses revealed no secondary phases and the structure was cubic for BTS50, BTS60, BTS70, and BTI50 with space group $Pm\bar{3}m$. The BTS20 sample was, however, hexagonal structured, with space group $P6_3/mmc$.[10]

To ensure fast equilibria at lower temperatures in the TG/TG-DSC measurements, all powders were ground for 1 h in a ball mill at 250 rpm in isopropanol prior to measurements.

3.2. TG and TG-DSC. TG and combined TG-DSC measurements were performed on all compositions using Netzsch Simultaneous Thermal Analyzers (STA): STA 449 F1 with a SiC furnace and a STA 499C Jupiter with water vapor furnace.

The STA 449 F1 was connected to a custom-built gas mixer unit, where $N_2(g)$ was dried by passing the gas through a $P_2O_5(s)$ column, while wet $N_2(g)$ was obtained by bubbling the gas through a saturated KBr solution at 26 °C, allowing water vapor partial pressures (p_{H_2O}) in the range from 3×10^{-5} to 0.03 atm. For practical reasons, the lowest employed p_{H_2O} in the TG measurements was 0.02 atm. The STA449C Jupiter was equipped with a water vapor generator, capable of producing a 0.15−1 atm H_2O atmosphere in the sample chamber.

The samples were dried at 1000 °C in bottle dry, flowing $N_2(g)$ for 30−60 min prior to TG/TG-DSC measurements. TG measurements of water uptake at low p_{H_2O} (0.02 atm) were performed isobarically in the temperature range from 1000 to 100 °C in steps of 50 °C with a ramp rate of 1 K/min, and the samples were equilibrated at each temperature for up to 12 h. TG-DSC measurements (and water uptake at higher p_{H_2O}) were performed isothermally by equilibration in dry, flowing N_2 at each temperature, followed by switching the $N_2(g)$ stream with $H_2O(g)$, ensuring an abrupt change in the atmosphere surrounding the sample. The TG and DSC signals of the sample were recorded simultaneously, and the sample was equilibrated in each hydration step.

Temperature and heat exchange sensitivity calibration curves were established by measuring the phase transition temperatures and enthalpies of standard materials supplied through the Netzsch calibration kit, spanning the employed temperature interval. To correct for buoyancy and changes in the heat capacity of the gas upon hydration, background measurements were made with empty crucibles using an identical temperature program and gas flow as for the measurements. The background was subsequently subtracted from all sample measurements.

3.3. Electrical Characterization. The electrical properties of $BaTi_{1-x}Sc_xO_{3-x/2}$ reported in this work are reproduced from results by Rahman et al.[9,10] where impedance spectroscopy within the frequency range from 4.5 MHz to 100mHz was used to extract the temperature dependence of the conductivity. For a more complete comparison of the hydration thermodynamics and transport properties of the Sc and In members, we also characterized the electrical properties of $BaTi_{0.3}In_{0.7}O_{2.65}$ (BTI70) in this work.

Electrical characterization was performed on a 20 mm BTI70 pellet prepared by sintering at 1400 °C for 12 h, achieving a relative density of ∼80%. The pellet was painted with circular Pt electrodes of diameter ∼1 cm on both sides using Pt ink (Pt ink 6926, Metallor UK). Electrical characterization was performed in a ProboStat measurement cell (NorECs, Norway) connected to a Solatron 1260 impedance spectrometer both with a constant ac frequency of 10 kHz and as a function of frequency in the range from 1 MHz to 1 Hz (impedance spectroscopy). Specific conductivities are calculated from sample geometry, while porosity corrections are not included. The electrical properties were measured isobarically as a function of temperature and isothermally versus p_{O_2} in the range from 10^{-5} to 1 atm with constant p_{H_2O} of 0.03 atm, and, moreover, versus p_{H_2O} in the range from 3×10^{-5} to 0.03 atm in oxygen. Finally, the effect of H → D isotope exchange on the bulk conductivity of BTI70 was investigated by bubbling the gas stream through a KBr−$D_2O(l)$ solution at 26 °C.

4. RESULTS AND DISCUSSION

4.1. Water Uptake and Hydration Thermodynamics. Figure 1 shows the water uptake of BTS70 measured by TG upon cooling at various p_{H_2O} (Figure 1a) and the BTS20−70 series measured in 1 atm $H_2O(g)$ (Figure 1b). The measurements were reproducible for all compositions, and XRD after measurements showed no signs of precipitation of secondary phases, even after prolonged exposures to 1 atm $H_2O(g)$. The weight change of the samples upon switching from dry $N_2(g)$ to dry $O_2(g)$ was negligible, and oxidation can therefore be neglected. The water uptake increases with decreasing temperature and with increasing p_{H_2O} (Figure 1a). For BTS70 the water uptake levels off at 0.33 mol H_2O/mol oxide below 200 °C for all p_{H_2O}, i.e., slightly lower than the theoretical

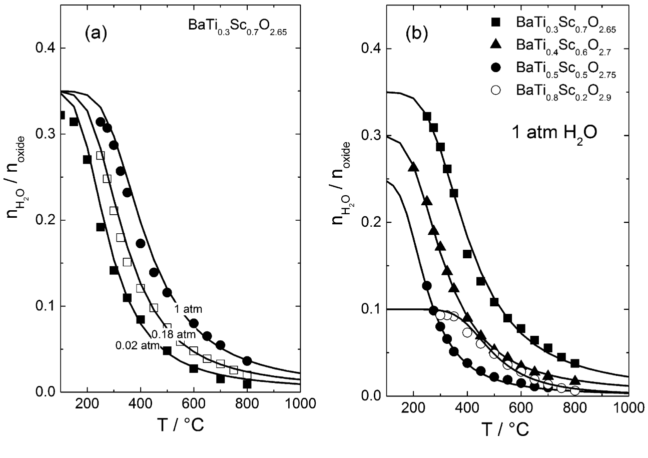

Figure 1. Water uptake measured by TG as a function of temperature upon cooling for (a) BTS70 with p_{H_2O} = 0.02, 0.18, and 1 atm and (b) BTS20−70 with p_{H_2O} = 1 atm. Solid lines represent curve fitting to the hydration model in eq 5.

saturation level of 0.35 mol H_2O/mol oxide. The water uptake further increases with increasing Sc concentration (Figure 1b), and both the temperature onset of hydration and saturation temperature increases in the same direction, reflecting more favorable hydration thermodynamics with increasing Sc concentration. The hexagonal BTS20 is, however, more fully saturated at higher temperatures than any of the cubic materials, reflecting more favorable hydration thermodynamics for the hexagonal member in this series of materials. Figure 2 compares the water uptake of BTS70 and BTS50 to those of their In analogues in the temperature range from 1000 to 250 °C in 1 atm $H_2O(g)$. While the hydration profiles of BTS50 and BTI50 are similar, the water uptake at a given temperature for BTS70 is significantly higher than that of BTI70. BTS70 contains significant levels of protonic defects even at 800 °C under this high p_{H_2O}. Close to the saturation limit, however, the water uptake of BTI70 increases more rapidly with decreasing temperature than that of BTS70. From XRD analyses, we note that while all Sc members and BTI50 retain their cubic structure even upon full hydration, fully hydrated BTI70 crystallizes in a tetragonal structure. Hydration of BTI70 is therefore not a single-phase reaction close to the saturation limit as also noted by Noirault et al.[20] and Quarez et al.[5] for similar compositions.

To elaborate on the hydration trends, we also performed combined TG-DSC measurements of hydration of BTI and BTS series of materials. Figure 3 shows the weight change of BTS70 upon hydration (Figure 3a) and the corresponding normalized DSC signal (Figure 3b) in the temperature range 300−800 °C. The relative weight gain increases with decreasing temperature and levels off after equilibration for 15 min at all temperatures. The heat flow is exothermic, and both the depth and the width of the peak increases with decreasing temperature, in correspondence with the increasing water uptake. The broadening of the peak reflects slower hydration kinetics at lower temperatures due to decreasing oxide ion and proton mobility. As in previous TG-DSC studies,[21] we observe a small baseline shift upon hydration. The choice of baseline affects the integrated area of the DSC peak, and all DSC signals in this work were, for consistency, integrated using a sigmoidal interpolation function between the "dry" and the "hydrated" baselines. The molar hydration enthalpy was determined from the integrated DSC area, and the total weight gain was interpreted as H_2O uptake. Figure 4 shows the hydration enthalpies of BTS70 measured between 250 and 800 °C. The hydration enthalpy becomes slightly more exothermic with decreasing measurement temperature, from around −80 kJ/mol at 800 °C to −90 kJ/mol at 250 °C. Kjølseth et al.[21] on the other hand observed that the hydration enthalpy of BZY was temperature independent. We suggest that the temperature effect on the hydration enthalpy observed here (Figure 4) may stem from the fact that the temperature dependency of the molar enthalpy of $H_2O(g)$ is not completely counteracted by that of the structurally bound water, i.e.

$$2H_{\mathrm{OH}_O^{\bullet}}(T) \neq H_{v_O^{\bullet\bullet}}(T) + H_{H_2O}(T) \qquad (6)$$

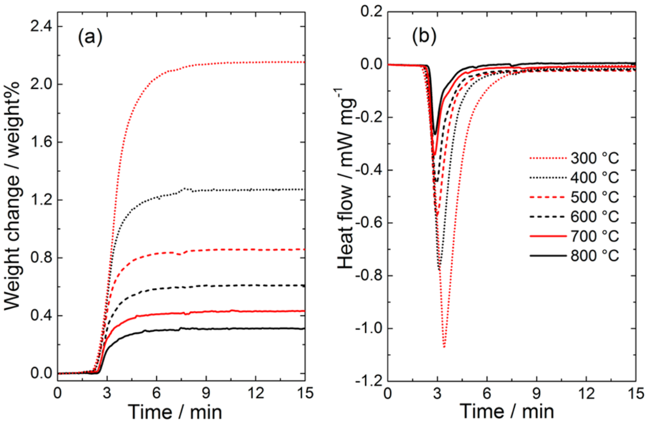

Figure 3. (a) Weight change and (b) the corresponding DSC signal (normalized with respect to the sample mass) of BTS70 upon hydration in the temperature interval 300−800 °C. Measurements are performed between flowing bottle dry N_2 and ~1 atm H_2O.

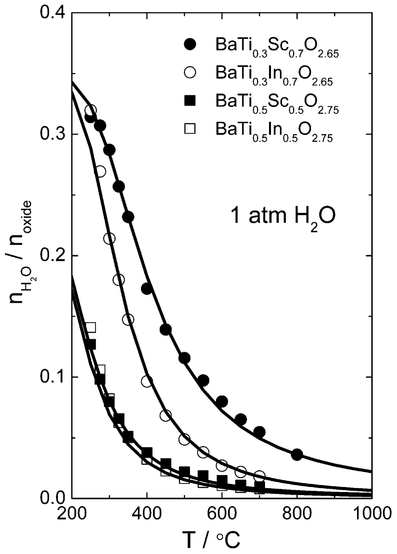

Figure 2. Water uptake of BTS50 and BTS70 compared with those of BTI50 and BTI70 and their measured by TG as a function of temperature upon cooling in the range 1000−250 °C in 1 atm H_2O.

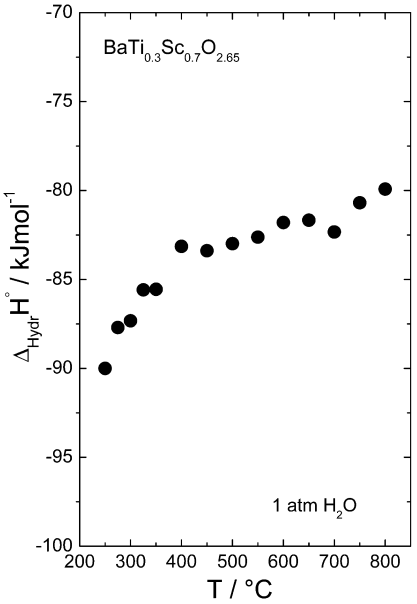

Figure 4. Hydration enthalpy of BTS70 measured by TG-DSC throughout the temperature range 250−800 °C by switching between dry $N_2(g)$ and 1 atm of $H_2O(g)$.

For consistency, we therefore only compare TG-DSC measurements performed at 500 °C for the remaining compositions.

Figure 5 compares the DSC signal and weight change of BTS70 and BTI70 upon hydration at 500 °C from dry N_2 to 1 atm H_2O. In accordance with the TG data in Figure 2, the water uptake of BTS70 is a factor of 2.5 higher than that of BTI70, despite their identical doping levels. This is also reflected in the DSC signals, with the heat exchange from BTI70 being significantly smaller than that of BTS70. The integrated DSC peak area and the mass change yield hydration enthalpies are -71 ± 2 and -83 ± 2 kJ/mol for BTI70 and BTS70, respectively. The hydration entropy corresponding to the measured enthalpy and water uptake may be estimated from to eq 5 and are -127 ± 2 and -92 ± 2 J/mol·K for BTI70 and BTS70, respectively.

Table 1 reports the hydration thermodynamics of all compositions as extracted by curve fitting of TG data to eq 5 and the hydration enthalpies from TG-DSC measurements at 500 °C and the corresponding hydration entropies. The solubility limits of H_2O are set to values derived from the nominal composition of the respective material. For BTS50 and BTI50, the enthalpies, and entropies, are in very good agreement with those from the TG data (Table 1) and reflect the fact that hydration of the former is slightly more exothermic than the latter. For higher In/Sc concentrations, however, the results from curve fitting of TG profiles and from TG-DSC deviate more. While TG indicates that it primarily is a less negative entropy contribution that is responsible for the more favorable hydration thermodynamics with increasing In/Sc concentration, TG-DSC clearly shows that the enthalpy also becomes more exothermic with increasing In/Sc concentration. This latter trend is opposite to the trend reported by Quarez et al.[5] for the BTI series derived from curve fitting of TG data. We suggest that this discrepancy is due to subtle trends in either $\Delta_{\mathrm{Hydr}}H°$ or $\Delta_{\mathrm{Hydr}}S°$ being easily overshadowed by changes in the other parameter, or the fact that the hydration thermodynamics in fact depend on the degree of hydration for these highly deficient oxide systems. The mismatch may also in part stem from the temperature dependency on the hydration enthalpy as observed with TG-DSC (Figure 4), which upon curve fitting of the TG data is averaged out over the employed temperature interval and thus included in the entropies. Nevertheless, for both the cubic 50 and 70 mol % Sc- or In-doped composition, the hydration enthalpy and hydration thermodynamics, in general, are more favorable for the scandates than the indates, and the compositional effect is strongest for the highest doping levels. Finally, in line with the water uptake measurements, the hydration enthalpy of the hexagonal BTS20 is more exothermic than for any of the cubic members. The more exothermic hydration enthalpy of the hexagonal BTS20 than the cubic members can be attributed to stabilization of protons in the hexagonal structure, either due to a larger extent of trapping by Sc or due to changes in the crystal symmetry itself.

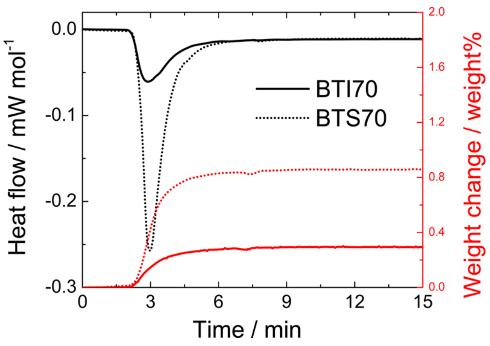

Figure 5. Relative weight change and heat flow normalized with respect to the number of moles of sample of BTS70 and BTI70 upon hydration at 500 °C. Measurements are performed by switching between flowing bottle dry N_2 and ~1 atm H_2O.

4.2. Electrical Transport Properties. *Characterization of BTI70.* All isobaric measurements for BTI70 were performed with a constant AC frequency of 10 kHz which, based on impedance spectra, reflects the bulk response throughout the temperature interval. Figure 6 shows the bulk conductivity of BTI70 as a function of inverse temperature in the range from 200 to 1000 °C, measured upon cooling in (Figure 6a) dry and wet O_2 or Ar and (Figure 6b) H_2O and D_2O hydrated air. The conductivity generally increases with increasing temperature and, moreover, with increasing p_{H_2O}. The functional p_{H_2O} dependency increases with decreasing temperature, reflecting hydration from water vapor, which increases the proton conductivity, in line with the TG and TG-DSC measurements (Figure 1−4). There is, in addition, a notable isotope effect on the conductivity (i.e., $\sigma_{H_2O} > \sigma_{D_2O}$) below 700 °C, a clear sign that protons contribute to and even dominate the bulk conductivity at lower temperatures. Further, there is an effect of p_{O_2} on the conductivity throughout the temperature interval that is essentially independent of the temperature. The increase in conductivity from inert to oxidizing conditions reflects a p-type contribution to the conductivity that is somewhat greater than that observed for BTI50,[7] but not as significant as that found for the BTS50−70 series.[10] However, as we did not observe any oxygen uptake due to oxidation in the TG/TG-DSC measurements, combined with the minor p_{O_2} dependency and the significant isotope effect, we conclude that electron holes are in minority concentration-wise, even in oxygen. The material therefore effectively behaves as an acceptor-doped oxide with oxygen vacancies and protons as dominating charge-compensating defects (eq 3).

Under inert atmospheres, the p-type contribution is minute and oxide ions and protons dominate the conductivity at high temperatures and dry atmospheres and low temperatures and wet atmospheres, respectively. The maximum proton conductivity is thus reflected by the plateau at 600−300 °C observed in wet Ar and amounts to $\sim 7 \times 10^{-4}$ S/cm at 450 °C, which is comparable to that reported by Quarez et al.[5,6] for the same composition.

BTS and BTI Systems. Due to the p-type contribution to the bulk conductivity under oxidizing atmospheres, we compare the total conductivities measured in dry and wet Ar only, where the p-type contribution is minimal. All bulk conductivities presented for the BTS50, BTS60, BTS70, and BTI50, are extracted from impedance data from refs 7, 9, and 10. For BTS60 and BTS70, the bulk and grain boundary contributions were overlapping at lower temperatures, and the reported bulk conductivities are therefore expressed with error bars reflecting the uncertainty in the bulk conductivity as emerging from deconvolution of the impedance data.

Figure 7 compares the bulk conductivity of BTI50 and BTS50 (Figure 7a) and BTI70 and BTS70 (Figure 7b) in dry and wet Ar from 150 to 1000 °C. All compositions exhibit a strong p_{H_2O} dependency at lower temperatures (below 700 °C),

Table 1. $\Delta_{Hydr}H°$ and $\Delta_{Hydr}S°$ of All Included Compositions Determined by Curve Fitting of Water Uptake Profiles from TG, Compared to the $\Delta_{Hydr}H°$ Measured Directly by TG-DSC at 500 °C and the Corresponding $\Delta_{Hydr}S°$

		extracted from TG profiles		TG-DSC	
composition	structure	$\Delta_{Hydr}H°$ (kJ mol^{-1})	$\Delta_{Hydr}S°$ (J mol^{-1}K^{-1})	$\Delta_{Hydr}H°$ (kJ mol^{-1})	$\Delta_{Hydr}S°$ (J mol^{-1}K^{-1})
$BaTi_{0.3}Sc_{0.7}O_{2.65}$	cubic	−56	−93	−83 ± 2	−92 ± 2
$BaTi_{0.4}Sc_{0.6}O_{2.7}$	cubic	−53	−102	−79 ± 2	−136 ± 2
$BaTi_{0.5}Sc_{0.5}O_{2.75}$	cubic	−55	−120	−57 ± 4	−127 ± 4
$BaTi_{0.8}Sc_{0.2}O_{2.9}$	hexagonal	−93	−143	−108 ± 2	−146 ± 2
$BaTi_{0.3}In_{0.7}O_{2.65}$	cubic	−68	−125	−73 ± 2	−127 ± 2
$BaTi_{0.5}In_{0.5}O_{2.75}$	cubic	−57	−132	−53 ± 5	−126 ± 5

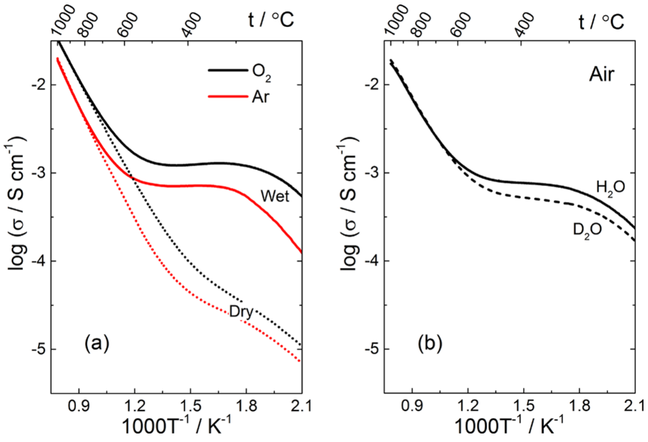

Figure 6. Bulk conductivity of BTI70 as a function of inverse temperature in (a) wet (solid), dry (dashed) O_2 (black), and Ar (red) and (b) in H_2O and D_2O humidified air.

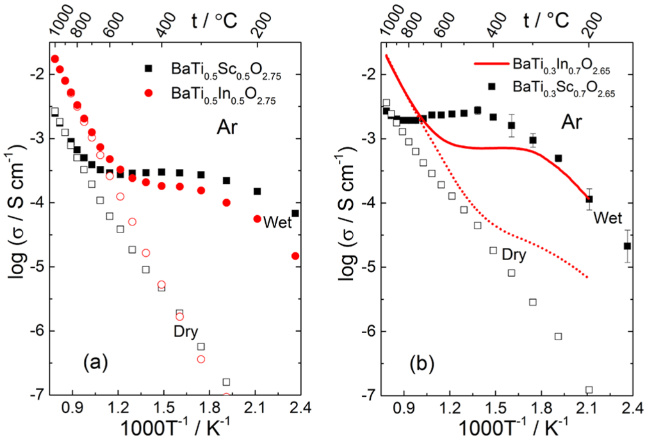

Figure 7. Bulk conductivity of (a) BTI50 and BTS50 and (b) BTI70 and BTS70 in dry and wet Ar from 150 to 1000 °C. Conductivity data of BTI50, BTS50, and BTS70 is obtained by deconvolution of impedance data from refs 7, 9, and 10, respectively. For BTS70, the bulk and grain boundary contributions were overlapping at lower temperatures, and the error bars represent uncertainties estimated from the impedance spectra.

reflecting a significant contribution from protons to the conductivity. Assuming that the maximum proton conductivity is given essentially by the "plateau" observed under wet conditions, the maximum is reached at slightly higher temperatures for both BTS50 and BTS70 than for their In analogues. The effect is larger for BTS70/BTI70 than BTS50/BTI50, in line with the more exothermic hydration enthalpy and higher proton concentration throughout the temperature interval for the Sc members (Figure 2). The conductivity of the Sc-members is also higher than that of the In-members at lower temperatures. The effect is largest for the BTS50/BTI50 compositions, despite their similar proton concentrations. Further, for both doping levels, the conductivity of the In members exceeds that of the Sc members at the very highest temperatures (i.e., the oxide ion and/or p-type conductivity), and simultaneously, the indium samples display higher activation energies.

Figure 8 compares the bulk conductivity of the BTS20−70 series measured in wet Ar in the temperature range from 1000 to 150 °C. The bulk conductivity at lower temperatures (which mainly reflects proton conductivity) displays a complex behavior with respect to the Sc concentration. Most notably, the conductivity of BTS20 is orders of magnitude lower than those of, for instance, BTS50, even at temperatures where its proton concentration is expected to be higher (Figure 1). This indicates that the hexagonal structure, which contains layers of face-sharing $(Ti/Sc)O_6$ octahedra, is unfavorable for proton mobility. On the basis of the more exothermic hydration enthalpy of the hexagonal BTS20 than the cubic members (Sc = 50−70 mol %), the low proton conductivity of BTS20 may be attributed to more strongly bound protons in the hexagonal phase than in the cubic materials. One may speculate whether this is a result of shorter O−O distances in the layers of face-sharing octahedra than in the corner-sharing network. As shown by DFT calculations of cubic vs orthorhombic

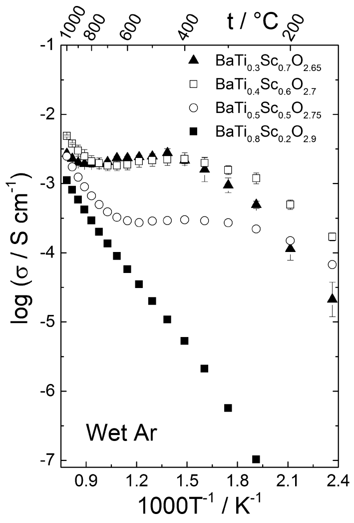

Figure 8. Bulk conductivity of the BST20-70 series in wet Ar. Reproduced from data in refs 9 and 10. For BTS60 and BTS70, the bulk and grain boundary contributions were overlapping at lower temperatures, and the error bars represent uncertainties estimated from the impedance spectra.

DOI: 10.1021/ic503006u
Inorg. Chem. 2015, 54, 2858−2865

perovskites in ref 2, a shorter O−O distance and thus a shorter OH···O distance stabilizes the protonic defect. Further investigations are nonetheless required to clarify this structural effect. The proton conductivity of BTS60 and BTS70 extends to higher temperatures than that of BTS50, in line with their more exothermic hydration enthalpy. At the lowest temperatures, however, the proton conductivities increase in the order BTS70 < BTS50 < BTS60, while the proton concentration increases in the order BTS50 < BTS60 < BTS70, indicating that the dopant concentration affects the proton mobility.

4.3. Thermodynamic Assessment of Conductivity Data.

Under the assumption that the contribution from p-type electronic conductivity is small in Ar, the total conductivity can be expressed in terms of the partial proton and oxide ion/vacancy conductivity

$$\sigma_{\mathrm{tot}} = \sigma_{\mathrm{H}^+} + \sigma_{\mathrm{v}_{\mathrm{O}}^{\bullet\bullet}} = \delta_{\mathrm{m}} F([\mathrm{OH}_{\mathrm{O}}^{\bullet}]\mu_{\mathrm{H}^+} + 2[\mathrm{v}_{\mathrm{O}}^{\bullet\bullet}]\mu_{\mathrm{v}_{\mathrm{O}}^{\bullet\bullet}}) \qquad (7)$$

with the mobilities given by

$$\mu_{\mathrm{i}} = \frac{\mu_{\mathrm{i}}^{0}}{T}\exp\left(-\frac{\Delta H_{\mathrm{m},i}}{RT}\right) \qquad (8)$$

where δ_{m} is the molar density of the material, μ_i^0 are the pre-exponential mobilities, and $\Delta H_{\mathrm{m},i}$ are the mobility enthalpies. The mobility parameters can therefore be determined by dividing the measured conductivities by the defect concentrations under temperature/atmospheric conditions where a single charge-carrier dominates. Oxide ions/vacancies dominate the conductivity under dry, inert conditions (i.e., dry Ar) at moderate temperatures, and their concentration is given by the constant acceptor concentration. Similarly, protons can be assumed to dominate the conductivity below ~450 °C under wet inert conditions, where their temperature-dependent concentration is given by the water uptake from the TG measurements.

The extracted proton mobilities of BTS50, BTI50, BTS70, and BTI70 are plotted as a function of inverse temperature in Figure 9, and the corresponding enthalpies of proton and oxygen vacancy mobility are compared in Table 2. The extracted proton mobilities display an Arrhenius-type behavior up to 350 °C, and in general increase in the order BTS70 < BTI70 < BTI50 < BTS50. While the proton mobility clearly increases with decreasing Sc/In concentration, the effect of Sc/In substitution on the mobility is seemingly also affected by the dopant concentration. This is reflected in the extracted $\Delta H_{\mathrm{m,H}^+}$ which are lower for BTI50/BTS50 than BTI70/BTS70, and higher for BTS70 than BTI70 while being lower for BTS50 than BTI50. The increasing $\Delta H_{\mathrm{m,H}^+}$ with increasing Sc/In concentration is opposite to the trend reported by Quarez et al. 5 for the BTI series, and indicates that the higher Sc/In concentrations lead to larger degree of proton trapping. $\Delta H_{\mathrm{m,v}_{\mathrm{O}}^{\bullet\bullet}}$ on the other hand increases with decreasing Sc/In concentration, and is also lower for the indates than the scandates. This indicates that the increasing Sc/In concentrations destabilize the oxygen vacancies, and that the indates bind oxygen vacancies more strongly than the scandates. The more exothermic hydration enthalpies with increasing Sc/In concentration may therefore be attributed both to stabilization of protons, and destabilization of oxygen vacancies, while the more exothermic hydration enthalpies of the scandates primarily is due to destabilization of oxygen vacancies.

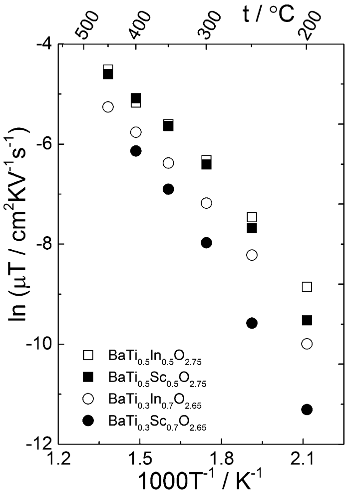

Figure 9. Proton mobility of BTS50, BTI50, BTIS70, and BTI70 as a function of inverse temperature estimated from the extracted bulk conductivities and proton concentrations according to eqs 7 and 8.

Table 2. Enthalpies of Proton and Oxide Ion Vacancy Mobility for BTS50, BTI50, BTS70, and BTI70 As Extracted from the Measured Bulk Conductivities and Proton Concentrations According to Eqs 7 and 8

	$\Delta H_{\mathrm{m,v}_{\mathrm{O}}^{\bullet\bullet}}$ (kJ mol^{-1})	$\Delta H_{\mathrm{m,H}^+}$ (kJ mol^{-1})
BTS50	95 ± 5	40 ± 5
BTI50	105 ± 5	49 ± 5
BTS70	66 ± 5	60 ± 5
BTI70	84 ± 5	59 ± 5

4.4. Hydration Thermodynamics of the BaTi$_{1-x}$M$_x$O$_{3-x/2}$ Series.

Sc generally results in more exothermic hydration enthalpies than In in the BaTi$_{1-x}$M$_x$O$_{3-x/2}$ series. The effect depends on doping level and can mainly be attributed to destabilization of oxygen vacancies with increasing doping level. The more exothermic hydration enthalpy of BaTi$_{1-x}$Sc$_x$O$_{3-x/2}$ with increasing Sc concentration is in line with the lower electronegativity of Sc vs Ti (1.4 vs 1.5 at the Allred−Rochow scale) and the general empirical correlation between hydration properties and electronegativity of ABO$_3$ perovskites.[1] For BaTi$_{1-x}$In$_x$O$_{3-x/2}$, however, the observed trend is opposite to what is expected empirically from the high electronegativity of In vs Ti. In fact, the correlation does not even predict hydration of the most In-rich compositions, thus reflecting its simplicity and unsuitability for such highly substituted materials. Within the cubic regime, $\Delta_{\mathrm{Hydr}}H°$ becomes more exothermic with decreasing Goldschmidt tolerance factor (i.e., with increasing Sc/In content), but as there are no changes in the crystal symmetry, we believe this trend actually reflects other fundamental properties, such as the oxide ion basicity or the oxide's stability.

In summary, the cubic oxygen-deficient BaTi$_{1-x}$M$_x$O$_{3-x/2}$ (M = In, Sc) series of oxides displays significant proton conductivity at intermediate temperatures, which is comparable to that of Y-doped BaZrO$_3$. Substituting In by Sc increases the proton conductivity, especially at higher temperatures, due to more favorable hydration properties. Scandium substitution stabilizes the cubic perovskite structure of the fully hydrated phases, and the BaTi$_{1-x}$Sc$_x$O$_{3-x/2}$ phases are also chemically stable with respect to hydroxide formation even at 1 atm H$_2$O down to 100 °C. Hence, the cubic BaTi$_{1-x}$Sc$_x$O$_{3-x/2}$ series of materials may find usage as electrolytes in applications such as steam electrolysis assuming the stability is retained during longer exposures.

5. CONCLUSIONS

From TG and TG-DSC measurements we have shown that the hydration thermodynamics of the $BaTi_{1-x}M_xO_{3-x/2}$ (M = In, Sc) series becomes more favorable with increasing Sc/In content within the cubic perovskite regime and is also more favorable for scandates than for the indates. In the Ti-rich limit, however, the scandates take on a hexagonal structure, with a profound effect on the hydration enthalpies and proton mobility. While the hydration enthalpies of the cubic BTS50−70 range from −57 ± 4 to −83 ± 2 kJ/mol, the hexagonal BTS20 displays a hydration enthalpy of −108 ± 2 kJ/mol. The hydration enthalpy trends are, as shown from conductivity measurements, closely related to the degree of trapping of protons and oxygen vacancies as reflected through their mobility enthalpies. For the cubic materials, the enthalpy of proton mobility increases with increasing Sc/In content, while that of oxygen vacancies follows the opposite dependency. We suggest that the more exothermic hydration enthalpy with increasing Sc/In content stems from stabilization of protons, and destabilization of oxygen vacancies. Finally, despite the tendency of the scandates to trap protons to a larger extent than the indates, their more favorable hydration thermodynamics increases their partial proton conductivity at the highest temperatures compared to the indates.

■ AUTHOR INFORMATION

Corresponding Author

*E-mail: torsb@kjemi.uio.no.

Notes

The authors declare no competing financial interest.

■ ACKNOWLEDGMENTS

The authors gratefully acknowledge the Norwegian Research Council for funding under the project “HydraThermPro” (project number 214252) and the Swedish Energy Agency (STEM).

■ REFERENCES

(1) Norby, T.; Widerøe, M.; Glöckner, R.; Larring, Y. *Dalton Trans.* **2004**, 3012−3018.

(2) Bjørheim, T. S.; Kuwabara, A.; Ahmed, I.; Haugsrud, R.; Stølen, S.; Norby, T. *Solid State Ionics* **2010**, *181*, 130−137.

(3) Jayaraman, V.; Magrez, A.; Caldes, M.; Joubert, O.; Ganne, M.; Piffard, Y.; Brohan, L. *Solid State Ionics* **2004**, *170*, 17−24.

(4) Jayaraman, V.; Magrez, A.; Caldes, M.; Joubert, O.; Taulelle, F.; Rodriguez-Carvajal, J.; Piffard, Y.; Brohan, L. *Solid State Ionics* **2004**, *170*, 25−32.

(5) Quarez, E.; Noirault, S.; Caldes, M. T.; Joubert, O. *J. Power Sources* **2010**, *195*, 1136−1141.

(6) Quarez, E.; Noirault, S.; Salle, A. L. G. L.; Stevens, P.; Joubert, O. *J. Power Sources* **2010**, *195*, 4923−4927.

(7) Rahman, S. M. H.; Knee, C. S.; Ahmed, I.; Eriksson, S. G.; Haugsrud, R. *Int. J. Hydrogen Energy* **2012**, *37*, 7975−7982.

(8) Jarry, A.; Quarez, E.; Joubert, O. *Solid State Ionics* **2014**, *256*, 76−82.

(9) Rahman, S. M. H.; Ahmed, I.; Haugsrud, R.; Eriksson, S. G.; Knee, C. S. *Solid State Ionics* **2014**, *255*, 140−146.

(10) Rahman, S. M. H.; Norberg, S. T.; Knee, C. S.; Biendicho, J. J.; Hull, S.; Eriksson, S. G. *Dalton Trans.* **2014**, *43*, 15055−15064.

(11) Norby, T. *J. Korean Ceram. Soc.* **2010**, *47*, 19−25.

(12) Prasanna, T. R. S.; Navrotsky, A. *J. Mater. Res.* **1993**, *8*, 1484−1486.

(13) Goodenough, J. B.; Ruiz-Diaz, J. E.; Zhen, Y. S. *Solid State Ionics* **1990**, *44*, 21−31.

(14) Jarry, A.; Quarez, E.; Kravchyk, K.; Joubert, O. *Solid State Ionics* **2012**, *216*, 11−14.

(15) Shin, J. F.; Hussey, L.; Orera, A.; Slater, P. R. *Chem. Commun.* **2010**, *46*, 4613−4615.

(16) Shin, J. F.; Orera, A.; Apperley, D. C.; Slater, P. R. *J. Mater. Chem.* **2011**, *21*, 874−879.

(17) Schober, T.; Friedrich, J.; Krug, F. *Solid State Ionics* **1997**, *99*, 9−13.

(18) Zhang, G. B.; Smyth, D. M. *Solid State Ionics* **1995**, *82*, 153−160.

(19) Jankovic, J.; Wilkinson, D. P.; Hui, R. *J. Electrochem. Soc.* **2011**, *158*, B61−B68.

(20) Noirault, S.; Celerier, S.; Joubert, O.; Caldes, M. T.; Piffard, Y. *Solid State Ionics* **2007**, *178*, 1353−1359.

(21) Kjølseth, C.; Wang, L.-Y.; Haugsrud, R.; Norby, T. *Solid State Ionics* **2010**, *181*, 1740−1745.

DOI: 10.1021/ic503006u
Inorg. Chem. 2015, 54, 2858−2865